

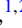



Film morphology and substrate strain contributions to ramp reversal memory in VO₂

Avital Fried ^{1,2} Elihu Anouchi ^{1,2} Gili Cohen Taguri,² Jonathan Shvartzberg ^{1,2} and Amos Sharoni ^{1,2,*}

¹*Department of Physics, Bar Ilan University, Ramat-Gan, 590002, Israel*

²*Institute of Nanotechnology and Advanced Materials, Bar Ilan University, Ramat-Gan, 590002, Israel*



(Received 17 August 2023; accepted 4 December 2023; published 9 January 2024)

The ramp reversal memory (RRM) effect that appears in thin films with temperature-driven insulator-metal transitions (IMTs) is a nonvolatile memory effect induced by a simple reversal of temperature ramping from heating to cooling during the phase-coexistence state of the IMT (when both metallic and insulating domains coexist). The memory of specific temperatures can be recorded by this ramp reversal, which appears as a resistance increase around the reversal temperatures. Previous studies showed RRM in VO₂, V₂O₃, and NdNiO₃, indicating it is a general effect in relevant systems. These studies indicate the RRM originates from an increase in the critical temperature around phase boundaries of the coexisting metallic and insulating domains during the temperature ramp reversal. However, the physical mechanism responsible for the T_C increase remains elusive. To enhance our understanding of the effect and provide clues to the underlying physics, it is crucial to understand the role of materials' properties, such as thickness, grain size, and choice of substrate, which have yet to be explored. We report the RRM properties in VO₂ thin films as a function of these parameters, namely choice of substrate, crystallographic properties, film thickness, and morphology. We find that films' grain size correlates with the RRM magnitude. The film thickness has a positive effect on the RRM, but at a much lesser extent. Interestingly, thinning films by a wet-etching process had almost no effect on RRM properties, indicating that the grain structure and interaction with substrate defined during deposition determines the RRM features. This was further corroborated by comparing of films grown epitaxially on sapphire with those grown nonepitaxially on SiO₂/Si substrates, where the latter show a fivefold increase in RRM magnitude. These findings support the hypothesis that strain (or strain gradients) and strain relaxation develop at phase-separated grain boundaries during the ramp reversal process, which controls the magnitude of the RRM effect.

DOI: [10.1103/PhysRevMaterials.8.015002](https://doi.org/10.1103/PhysRevMaterials.8.015002)

I. INTRODUCTION

The ramp reversal memory (RRM) is a recently discovered memory effect observed in thin films of correlated transition-metal oxides (TMOs) with temperature-driven insulator to metal transitions (IMTs) [1–3]. The memory manifests as a nonvolatile resistance increase of the film, but only at a specific temperature or temperatures, following a rather simple writing protocol. An efficient heuristic model, capable of qualitatively explaining various properties of the effect, was previously suggested. However, a rigorous explanation of the source of this memory effect is still lacking. To gain further insight into the effect and provide guidelines to development of a theory for the RRM, more quantitative measurements are needed, which is the main goal of this study.

Currently, the materials measured to exhibit the RRM effect include VO₂, V₂O₃, and NdNiO₃ [1–3]. These materials share common characteristics, which are understood to be relevant for the emergence of the RRM and include the following: (1) They undergo a first-order phase transition, in this case a temperature-driven IMT [4,5]. (2) The phase transition is accompanied by a structural transition concurrent with the IMT. Both vanadates show a structural transition,

in VO₂ from low-temperature monoclinic structure to high-temperature tetragonal [6,7], and in V₂O₃ from corundum to monoclinic [8]. The nickelate has a symmetry lowering during the IMT, from orthorhombic to monoclinic [9,10]. (3) All materials exhibit hysteresis behavior during the transition, observed as different R vs T curves during heating and cooling measurements. (4) The IMT is characterized by spatial phase separation, where during the transition the system contains two distinct and spatially separated metallic and insulating phases [11–13]. (5) The critical temperature of the phase transition can be modified by various changes in the material properties or external stimuli, including metallic doping [14], ionic doping [15,16], deposited thickness [17,18], or strain [9,19–21].

Figure 1 illustrates key aspects of the RRM properties and the memory-writing protocol. The sample is a VO₂ thin film deposited on C-cut sapphire. Note that this is a different substrate than that used in previous reports of RRM, where the effect was measured for VO₂ deposited on R-cut sapphire [1,2]. The protocol starts with heating and cooling the sample between different temperatures covering the entire hysteresis range (from the fully insulating state to the fully metallic state and back), from 328 to 358 K in this case. See Fig. 1(a) for the R vs T plot, and Fig. 1(b) showing the temperature change over time— y axis is time and x axis is temperature; color coding of the loops is the same in both figures. Initially, the sample is

*amos.sharoni@biu.ac.il

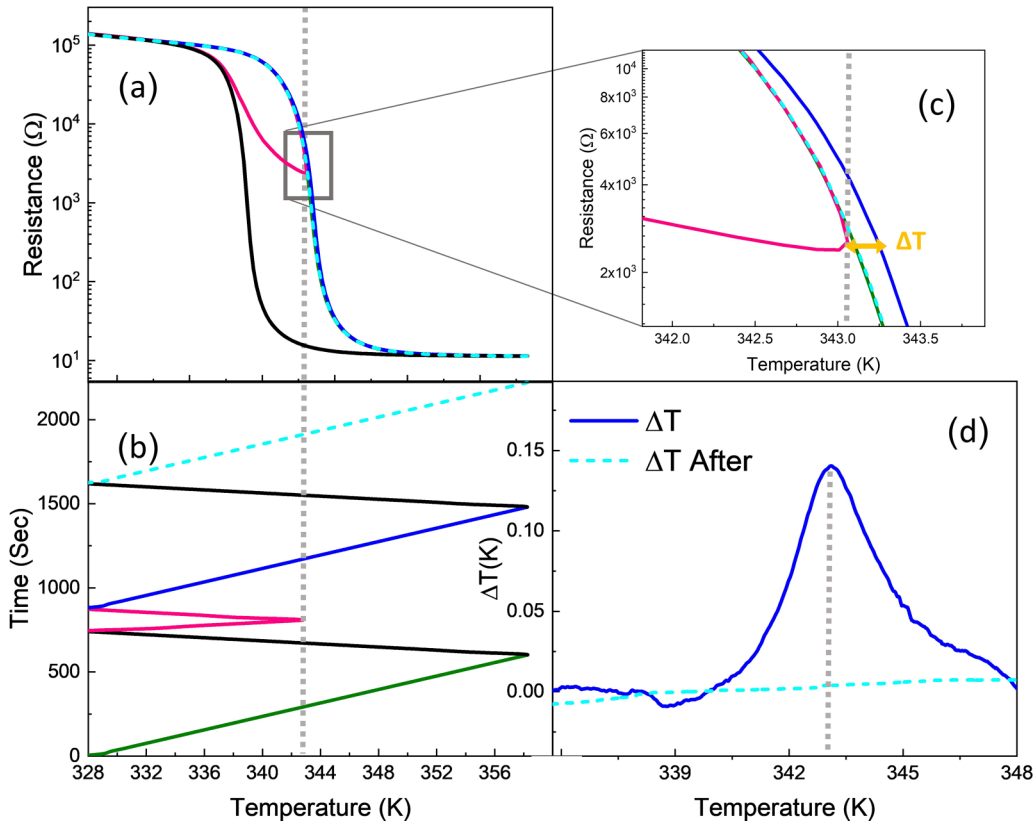


FIG. 1. RRM effect measurement on a 180-nm VO₂ film grown on a C-cut sapphire substrate. (a) R vs T and (b) time vs temperature measurements of the RRM writing and reading sequence, aligned on the same temperature x axis. Green: heating curve of the first ML; black: cooling curve of the first ML; pink: RL; blue: heating curve of the second ML; black: cooling curve of the second ML; dashed cyan: heating curve of the third ML. The dashed gray line in all panels marks the T_R of 342.7 K. (c) A zoom-in section of (a), focusing on the T_R region. ΔT is marked. (d) Plot of ΔT vs T for the heating curve right after the RL (blue) exhibiting a maximum at T_R , and for the following heating curve, dashed cyan line, where the peak is erased.

heated to a fully metallic state and then cooled down to a fully insulating state, forming a major loop (ML). Subsequently, the sample is heated to a specific temperature called the “reversal temperature,” T_R , which is at an intermediate temperature, during the spatially phase-separated state [marked by a vertical gray dashed line in Figs. 1(a) and 1(b)] [11–13]. Then, the sample is cooled back to the insulating state, thus forming a “reversal loop” (RL). This completes a memory writing. Then the sample is heated again to a fully metallic state, which is the memory-reading stage (it also erases the memory when heating above T_R , as further discussed below). Comparison between the cyan and the blue heating-resistance curves in Fig. 1(c)—the heating curves before and after the RL—shows that the resistance changes considerably near T_R . A physically meaningful way to analyze the effect, shown in Ref. [3], is to calculate for each temperature the temperature shift required to return to the original resistance, marked in Fig. 1(c) as ΔT . In Fig. 1(d) we plot ΔT vs T , blue curve, showing a peak at exactly T_R , a hallmark of the RRM effect. Then, in the next heating measurement (after cooling, of course) the original resistance is recovered, and the memory is erased. This can be seen by the dashed cyan line in Fig. 1(c) and by the dashed cyan line in Fig. 1(d), where the relative ΔT vs T measurement shows the peak disappearing. For a detailed

explanation and additional properties of the RRM, please refer to Ref. [1].

We recap the heuristic model that was hypothesized in Ref. [1] that qualitatively captures all reported RRM features: (1) During the temperature ramp reversal (at T_R) there are spatially separated insulating and metallic domains [12,13,22,23]. (2) The hypothesis is that the insulator-to-metal transition temperature of the phase boundaries, between the spatially separated insulating and metallic domains, increases due to this ramp reversal. We refer to these phase boundaries with increased IMT temperature as scars. (3) Thus, during the following resistance measurement there is a delay in the advancement of the transition, which appears as an averaged temperature delay in the transition—hence the measurement of ΔT is a meaningful estimation to the magnitude of RRM effect. (4) This delay in the transition also manifests as a resistance increase, but this measurement is highly affected by the resistivity and transition properties of the IMT. (5) Finally, when the temperature is increased further above the reversal temperature, the previous scars are “healed” and the memory is erased [1].

While the heuristic model successfully describes the fundamental characteristics of the RRM, a physical model is still lacking. To develop a comprehensive theory, it is crucial to

gain insight into how the RRM is quantitatively determined, i.e., what are the factors that influence the magnitude of the RRM. Note that based on our heuristic model, the magnitude can be influenced either by increasing the amount of scarring in the sample (or the width of each scar), or by increasing the magnitude of local ΔT induced by each individual scar. We have previously demonstrated that performing more RLs in a specific sample results in an increase in ΔT due to production of more scars. However, this does not answer how changing systems' properties affects the scars' properties, which is needed to understand the underlying mechanism.

It is well established that the IMT transition properties in TMO, and specifically in VO₂ thin films, are modified by strain [20,24,25]. One plausible option is that the RRM is related to strain coming from lattice mismatch between the film and the substrate [25–27]. In this case, by modifying the films' thickness, the relative role of substrate interactions and bulk energies will change. Measuring the effect of the interaction with the substrate can also be measured by changing the substrate. Additionally, strain can be stored in grain boundaries. In this case it is not clear if larger grains enable more strain energy, and a larger effect on ΔT , or if smaller grains result in more scars that increase ΔT . Note that changing film's thickness or growth substrate can change additional properties, such as grain size, shape, or growth orientation. Thus, care must be taken when analyzing the different contributions.

In this study we aim to reveal contributions of the aforementioned system parameters on the magnitude of the RRM, and the source of these changes. That is, do we have more scars or a larger ΔT produced by each scar? And, what are the system parameters which are contributing to the effect? We find that depositing films to increasing thicknesses does show an increase in the RRM magnitude. However, reducing film thickness by a wet-etching process has almost no effect on RRM properties. Comparing VO₂ films grown epitaxially on C-cut sapphire with those grown nonepitaxially on SiO₂/Si substrates reveals a fivefold increase in the RRM effect in the nonepitaxial growth, more than any other contributing factor. We discuss in depth the insights provided from these findings and their implications for our understanding of the mechanism underlying the RRM.

II. RESULTS

The paper is organized as follows: In Sec. II A we explain how we acquire a quantitative measurement of the RRM so we can compare different samples. Then we show results from three sets of measurements, including RRM and structural properties: Section II B shows VO₂ deposited on C-cut sapphire substrates to different thicknesses (60, 100, 180, and 340 nm.) Section II C compares properties of 180-nm-thick VO₂ films (deposited on the C-cut substrates) that are wet etched [28,29] to different thicknesses (original 180-nm and 134-, 94-, and 23-nm etched films). Section II D shows properties of VO₂ films deposited on a SiO₂/Si substrate to thicknesses of 60 and 120 nm, and compares them to the films deposited on C-cut sapphire substrate. Finally, in Sec. III we discuss all measurements together, and conclude.

A. Evaluation for the RRM magnitude

To evaluate the magnitude of the RRM effect in the different films we performed an RRM writing and reading protocol, with a single RL for many different reversal temperatures, throughout the entire transition. In Fig. 2(a) we exemplify the measurement for the 180-nm VO₂ film atop C-cut sapphire. Over 30 different T_R s were measured for each film. RLs of two different reversal temperatures are marked in the figure with distinct colors.

Next, we analyze the ΔT vs T plot for each reversal temperature. We note that VO₂ is known to exhibit a time-dependent increase in resistance while in its insulating state, which is unrelated to the RRM (see Supplemental Material of Ref. [1]). This may introduce an unwanted offset in the ΔT analysis which will skew the results. We developed a procedure to separate the time-dependent effects from the RRM, which is detailed in our Supplemental Material (SM), Sec. S1 [30]. In Fig. 2(b) we plot the ΔT vs T curves for the different reversal temperatures after removing the time-dependent effect. Each measurement shows a maximum in ΔT that correlates with its reversal temperature, marked by a dot. We exemplify the curves for the color-coded reversal loops of Fig. 2(a). At reversal temperatures below the beginning of the IMT there is no peak in the ΔT measurement, as expected. The ΔT maxima increase with the reversal temperature up to some maximum, and then decrease. At higher reversal temperatures the measurement becomes noisy, and we are not able to resolve the peak above 348 K. As mentioned above, the ΔT amplitude should be related to the magnitude of the RRM effect [3]. In this case the change in ΔT magnitude is attributed to a change in the amount of phase boundaries during the IMT, due to the percolation nature of the transition [23,31], resulting in changes to the amount of scarring [3]. Thus, at the vicinity of the percolation threshold one would expect a maximum in the RRM magnitude. This issue will be further elaborated upon in the Discussion, Sec. III. In general, the graph of ΔT peaks vs reversal temperature is a fingerprint of the RRM effect in the sample, and we can compare it between different samples.

B. VO₂ deposited to different thicknesses

VO₂ thin films were sputter deposited on C-cut sapphire substrates with thicknesses of 60, 100, 180, and 340 nm. The deposition is done by rf-magnetron sputtering from a V₂O₃ target in our AJA Orion chamber, with base pressure of 1×10^{-8} Torr. We used the same deposition protocol described in Ref. [29], but on a C-cut sapphire instead of R-cut sapphire. The characteristics are presented in Fig. 3. Figure 3(a) shows R vs T measurements of the different samples (thickness appears in the figure). All films exhibit an IMT, but with some variation in magnitude of resistance change, width of transition, and hysteresis. The temperature coefficient of resistance ($\text{TCR} = \frac{1}{R} \frac{dR}{dT}$) vs T is shown for the heating branch in Fig. 3(b) (color coding marked in image). The transition magnitude increases with increasing thickness, except for the 340-nm sample, where the magnitude decreases. X-ray diffraction (XRD) measurements, plotted in Fig. 3(c), reveal that all samples exhibit epitaxial growth in the (002) direction [32,33]. The VO₂ (002) peak approaches the value

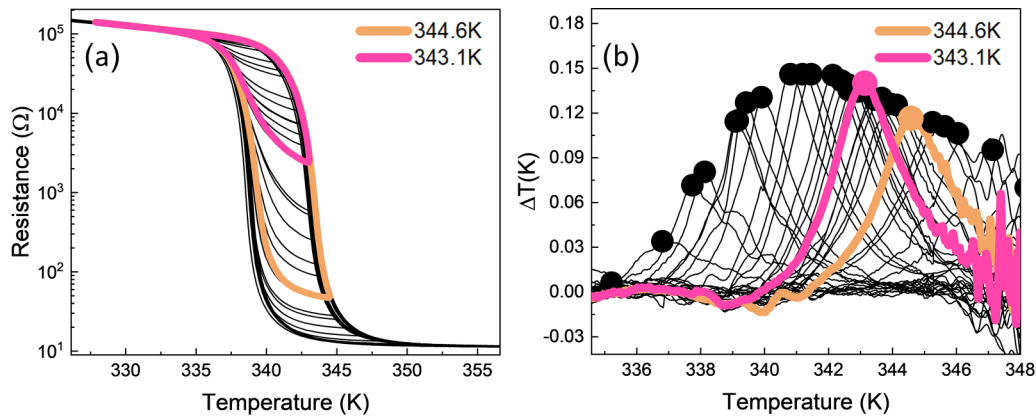


FIG. 2. (a) R vs T from many ramp reversal measurements of different reversal temperatures. Two specific reversal temperatures, 344.6 and 343.1 K, are highlighted with distinct colors. (b) ΔT analysis for each reversal temperature. The peak of each ΔT curve corresponding to its reversal temperature is marked with a black dot. The curves and the dots of the 344.6 and 343.1 K reversal temperatures are colored consistently with (a).

of bulk VO_2 with increasing thickness [Fig. 3(d)]. Atomic force microscopy (AFM) measurements of the samples are presented in Figs. 3(e)–3(h); film thickness is marked in each. The inset in Fig. 3(d) plots the average grain size of the films vs thickness, calculated from the AFM images. The grain size increases with thickness, as expected [34,35], except for the 340-nm film, where the grain size is smaller than anticipated. We will discuss this point further in Sec. III.

Figure 4 shows a comparison of the ΔT peak vs reversal temperature for the VO_2 films deposited to different thicknesses. The temperature axis is shifted to each film’s TCR maximum, which corresponds with the center of the IMT. All films present the aforementioned behavior, where the ΔT peak first increases with reversal temperature, reaches a

maximum, and then decreases. For all films, the maximum value of ΔT occurs at lower reversal temperatures than the TCR’s peak. We compare the maximum ΔT measurement among the different films as a coarse indicator to the RRM effect in that film. In Figs. 4(b)–4(d) we compare the ΔT peak maxima of different films with different film properties; Fig. 4(b) is vs thickness, Fig. 4(c) is vs TCR maximum, and Fig. 4(d) is vs grain size. For the samples deposited to different thicknesses, one can see that the maximum value of ΔT increases with thickness, except for the thickest 340-nm film, where the maximum is lower. The difference in this film is that the grain size is much smaller and the TCR is lower. We note that this is probably due to some difference in the deposition of this specific film, and not a feature of thick films. However,

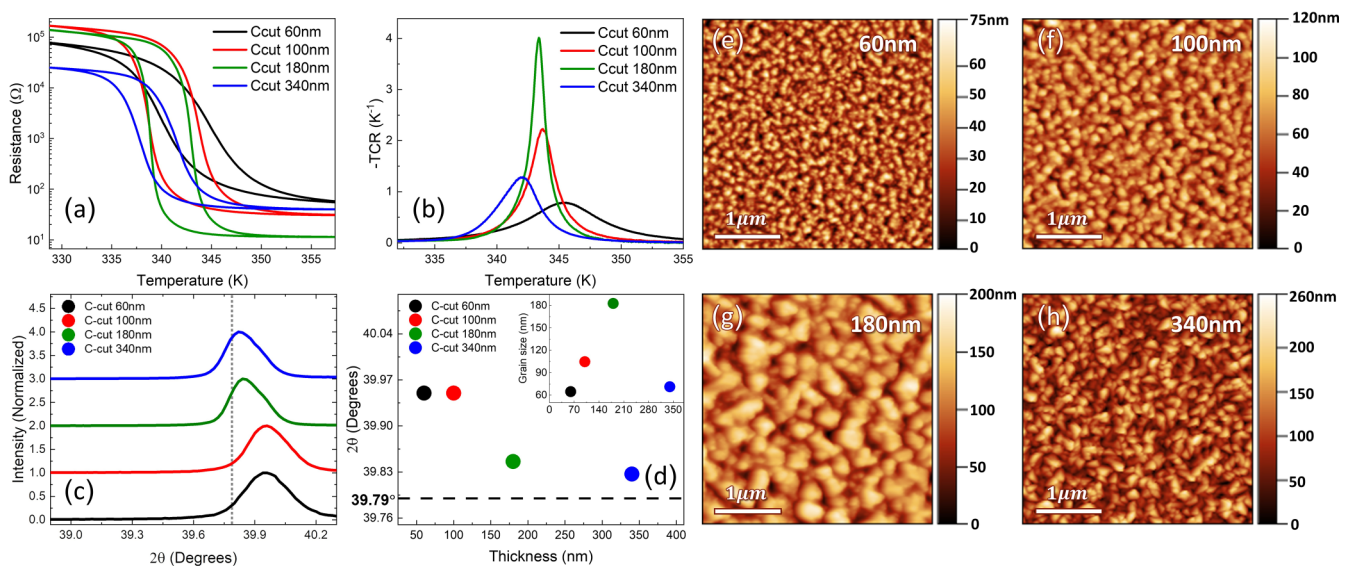


FIG. 3. Characterization of VO_2 films deposited to different thicknesses: 60 nm: black; 100 nm: red; 180 nm: green; and 340 nm: blue. (a) R vs T , (b) TCR vs T , and (c) XRD θ - 2θ measurements of the films. The θ - 2θ measurement is focused on the VO_2 (002) peak area. The intensity values are normalized to 1. The VO_2 bulk value is marked, both in (c) and (d). (d) θ - 2θ measurements of the angle of the VO_2 (002) peak as a function of deposited thickness. The peak approaches the VO_2 bulk value with increasing thickness. The inset in (d) is the grain size of films vs the deposited thickness. The crystal size is calculated from the AFM measurements of the films (e)–(h). More about the grain-size calculation can be found in the SM, Sec. S2 [30] (see also Refs. [46,47] therein).

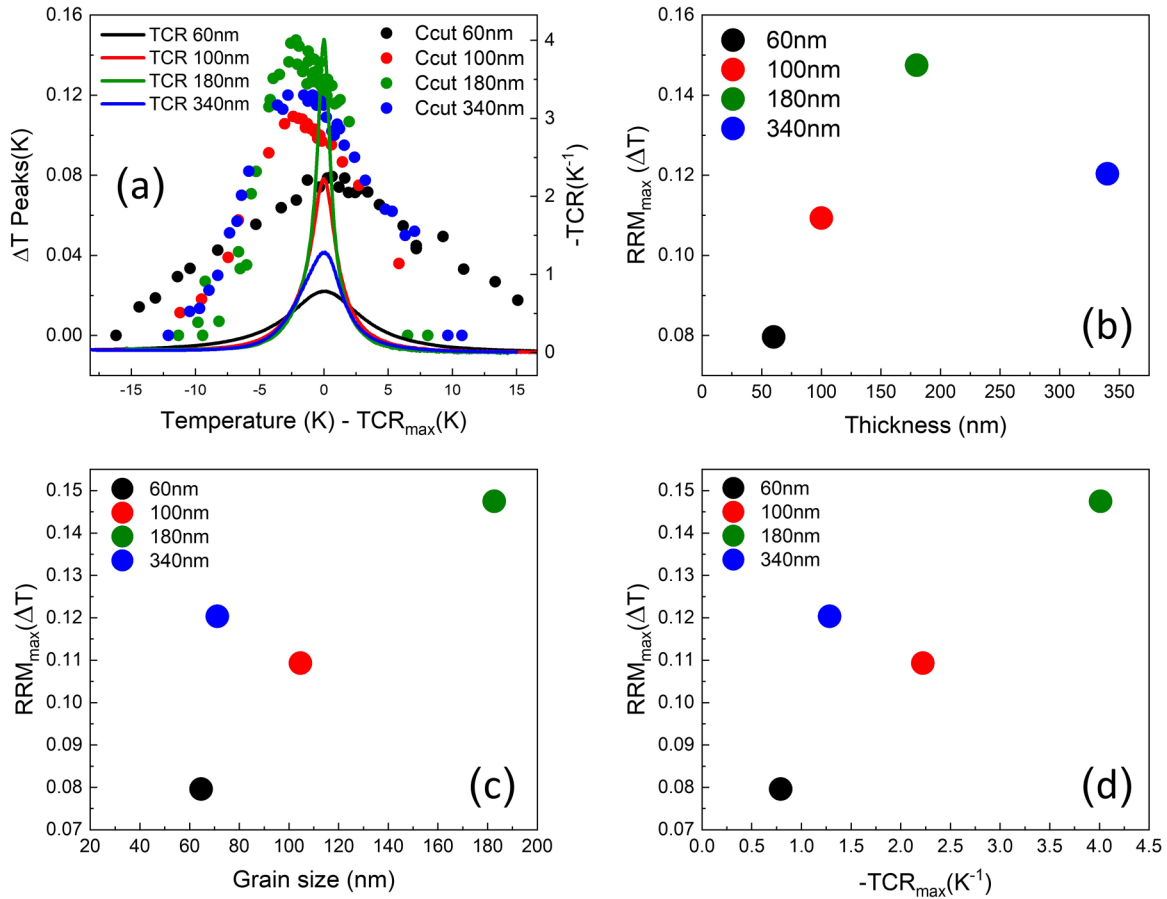


FIG. 4. (a) Dots are the ΔT maxima vs T_R for the films with different deposited thicknesses, left y axis. Lines are the negative values of the TCR vs temperature of each film, right y axis. Both the TCR and the RRM curves are shifted to the peak of the TCR of each film. (b)–(d) ΔT peak maxima of the films vs different film properties; (b) vs thickness, (c) vs TCR maximum, and (d) vs grain size. The grain-size calculation was done based on the AFM images.

it provided us with much insight into the RRM, as will be elaborated in the Discussion, Sec. III. We observe a correlation between the grain size and the magnitude of the maximal ΔT , except for the 340-nm again, and the main difference is that the sample is thicker. A similar trend for the effects of deposition thickness was observed for VO_2 deposited on R-cut sapphire; see SM, Sec. S5 [30]. In the following section we continue to overview all results before getting into further discussions and conclusions.

C. VO_2 wet etched to different thicknesses

VO_2 films of different thicknesses were prepared by thinning the 180-nm film to different thicknesses via a wet-etching process. This technique was chosen since it was shown to maintain the transport properties, oxygen stoichiometry, and crystal structure of the films [28]. Specifically, VO_2 was deposited on a large C-cut sapphire substrate that was then broken into several pieces. Each piece was immersed in a NaOH solution for a different time, following the process described in Ref. [28] (but with NaOH concentration of 4000 μMol NaOH in 100 ML). This resulted in films with different thicknesses and somewhat different surface morphologies. The characteristics of the films are presented in Fig. 5.

The R vs T curves for the different films show an increase in resistance with decreasing film thickness, but with almost no broadening of the transition, except for the thinnest 26-nm sample; see Fig. 5(a). The TCR and θ - 2θ measurements of these films are exhibited in Figs. 5(b) and 5(c), accordingly. The XRD measurements demonstrate an epitaxial growth in the (002) direction of all samples and exhibit nearly the same angle for the VO_2 (002) peak (as expected), and only a slight relaxation in strain with etching.

As shown in the AFM images of the films [Figs. 5(d)–5(g)], the thickness profile measurements and cross-sectional scanning electron microscopy images (shown in SM, Secs. S3 and S4 [30]), the films do not exhibit homogeneous thickness across their surface. The average thicknesses were measured to be 177 nm (38.5), 134 nm (52.6), 94.4 nm (43.5), and 23 nm (24.9), where the number in parentheses is the standard deviation. Note that the nominal thickness analyzed for the nonetched film agrees with the thickness measured from a rate monitor during deposition, indicating the reliability of the analysis. Interestingly, the 26-nm film exhibits areas in which the etching process resulted in voids where the VO_2 is etched down to the substrate (see SM, Sec. S3 [30]).

The RRM magnitude measurement (analysis of ΔT peak maxima vs reversal temperatures) for all the etched films is presented in Fig. 6(a). Each curve is shifted to the film's TCR

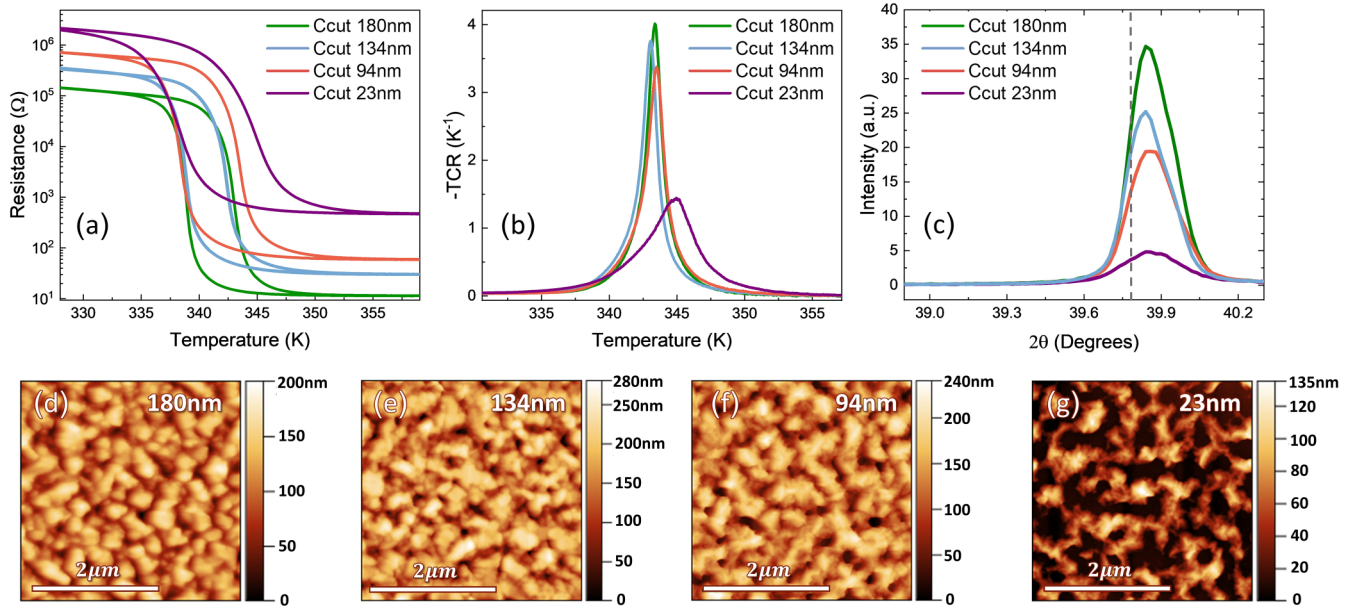


FIG. 5. (a) Characteristics of VO₂ films deposited with a thickness of 180 nm, which were subsequently etched to different thicknesses of 134, 94, and 23 nm. (a) R vs T , (b) TCR vs T , and (c) XRD θ - 2θ measurements of the films. The θ - 2θ measurement is focused on the VO₂ (002) peak area. It is seen that the peak is at the same position for all films. (d)–(g) AFM measurements of the different films. See SM, Sec. S3 for AFM zoom-ins and thickness profile measurements.

peak. Similar to films deposited to different thicknesses, the maximum value of the ΔT peaks occur at lower temperatures than TCR peaks. However, now the magnitude of the ΔT peaks is very similar for the different thicknesses (and different morphologies), and slightly increases as the films are further thinned (while previously the magnitude was smaller for thinner films). This increase is smaller compared to the trend observed in the films deposited to different thicknesses. A similar trend for the effects of etching was observed for VO₂ deposited on R-cut sapphire; see SM, Sec. S6 [30].

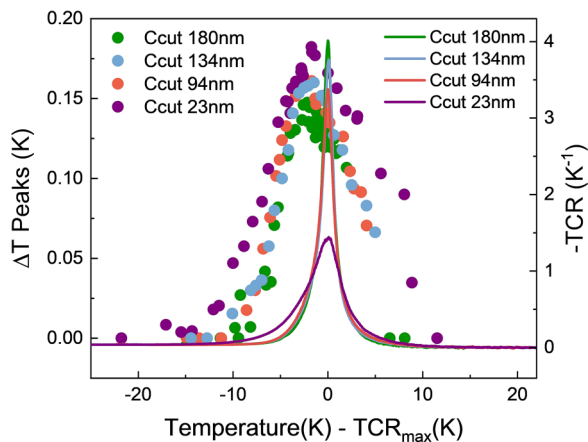


FIG. 6. (a) The ΔT maxima vs T_R of VO₂ films etched to different thicknesses. The left y axis shows the RRM magnitude, while the right y axis shows the negative values of the TCR vs temperature of each film. Both the TCR and the RRM curves are shifted to the peak of the TCR of each film.

D. VO₂ deposited on SiO₂/Si substrates

VO₂ films with thicknesses of 60 and 120 nm were sputter deposited on Si (100) substrates with a 750-nm-thick thermally grown SiO₂ layer using the same deposition process described above. Figure 7 shows the R vs T [Fig. 7(a)], TCR [Fig. 7(b)], θ - 2θ [Fig. 7(c)], and AFM measurements [Figs. 7(d) and 7(e) for the 60-nm film and Figs. 7(f) and 7(g) for the 120-nm film]. The magnitude of the resistance change during IMT for both films is smaller than that of the VO₂ films deposited on C-cut sapphire substrates, and the transition and hysteresis are wider. The 60-nm film exhibits a larger resistance change than the 120-nm film [Fig. 7(a)]. Both films do not grow via lattice matching and do not have preferred in-plane orientation (nonepitaxial). The films show a preferred out-of-plane growth along the (011) direction. The 120-nm-thick film is multiphase, where V₆O₁₃ and V₄O₉ peaks are also present, which sometimes occurs and has been previously reported [36]. The existence of phases in addition to VO₂ explains why the IMT resistance change is smaller in this film. AFM images show larger grains for the 120-nm film.

The RRM magnitude measurement (ΔT peak maxima vs reversal temperature) for VO₂ deposited on SiO₂/Si substrates, along with those deposited on C-cut substrates of different deposition thicknesses, are presented in Fig. 8. Each curve is shifted to its film’s TCR peak. VO₂ deposited on SiO₂/Si substrates exhibits a shift between the ΔT peak maxima and the TCR peak that is much larger than for films deposited on sapphire; compare the dashed purple curve (120 nm on SiO₂) and the blue dashed curve. Remarkably, the RRM magnitude of VO₂ films deposited on SiO₂/Si substrates is notably larger compared to that of those deposited on

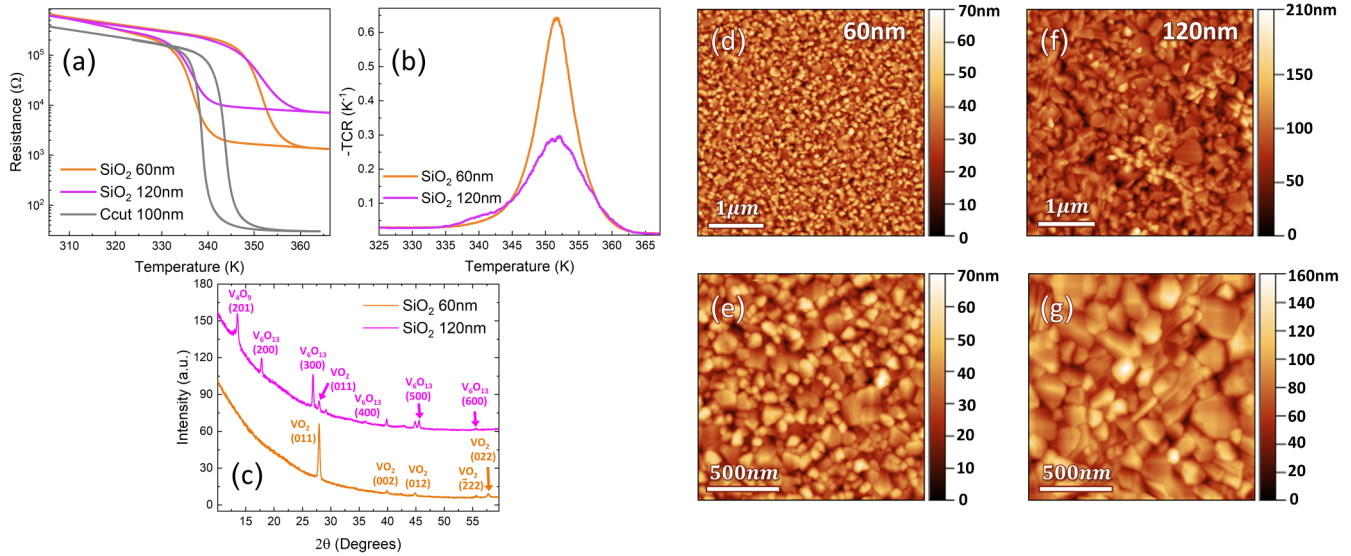


FIG. 7. Characteristics of 60- and 120-nm VO₂ films deposited on silicone substrate with a thin (750-nm) layer of oxide on top. (a) R vs T , (b) TCR vs T , and (c) XRD θ - 2θ measurements of the films. The θ - 2θ measurement in (c) reveals that the 60-nm film contains only VO₂, while the 120-nm film contains VO₂, V₆O₁₃, and V₄O₉. (d)–(g) The AFM measurements of the different films. (e) and (g) are zoom-ins of (d) and (f), accordingly.

C-cut sapphire, and this difference is particularly pronounced in the 120-nm film.

III. DISCUSSION

As mentioned in the Introduction, there are two scenarios that may affect the magnitude of the RRM signal under the heuristic scars model. One scenario is a change in the amount of scarring in a sample. If a reversal loop results in more scars—the magnitude of the RRM will increase, and

vice versa [3]. A second scenario is that each individual scar may induce larger delay in the (local) transition temperature. Here, even if the amount of scars remains the same, the RRM magnitude will increase.

There are different sample properties that might contribute to the RRM magnitude. Let us consider the contribution of grain size. It is known that the grains size has an influence on the IMT properties [34,37,38], making it a plausible candidate for affecting the RRM. However, usually the grain size of the film is correlated with the film’s thickness when deposited under identical conditions [34], so it is hard to separate these two effects. We were lucky in this study; some unintentional change in the deposition condition (possibly substrate temperature) resulted in a thick VO₂ film but with small grains. A reasonable assumption is that spatially separated phase boundaries occur at grain boundaries [22,39]. So, a film with smaller grains may result in a larger amount of grain boundaries and scars. While this may be correct, our measurements show that the RRM signal is actually smaller in films with smaller grains (see Fig. 4), meaning the source of the increase of the ΔT is not due to an increase in the amount of scars, but rather due to a larger shift in the ΔT of each individual scar. So, films with larger grains result in scars with a larger change to the local critical temperature. The 340-nm film has grains similar in size to that of the 100-nm film. Here, it is conceivable that the three-dimensional granular structure in this thick film does contribute to more grain boundaries, and thus the magnitude of the RRM in the 340-nm film is larger than in the 100-nm film, but smaller than the 180-nm film that has larger grains. This conjecture is further corroborated by the fact that etching a film to smaller thickness did not change the ΔT measurements much, where correspondingly, there was not much change in the grain structure. There is some correlation between the magnitude of the TCR and the RRM in the films deposited to different thickness, but this is clearly not the case in the wet-etched films, or the films deposited on

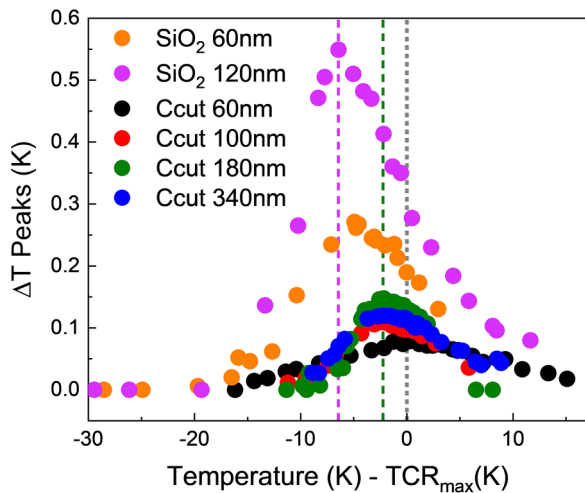


FIG. 8. The ΔT maxima vs T_R of VO₂ films, deposited to different thicknesses on C-cut sapphire and on SiO₂; see legend in figure for color coding. The T_R is shifted by the peak of the TCR of each film. The maximum values of the RRM curve of the 340-nm VO₂ deposited on C-cut sapphire and of the 120-nm VO₂ deposited on SiO₂ are marked with dashed lines (blue and purple, accordingly), indicating the distance from the TCR peaks (at zero, gray dotted line).

the SiO₂/Si substrate, so TCR is not related to the RRM (more likely TCR correlates with grain size).

We next discuss interactions with the substrate. We observe two main outcomes. First, for the two growth substrates-VO₂ films deposited to larger thicknesses showed an increase in RRM signal, related to the larger grains in thicker films (as discussed above). And, etching the films postdeposition to thinner films had nearly no effect on the RRM signal. Only when films were thinned even further and the structure started to separate into islands was a change measured, where the ΔT magnitude increased. This indicates that the structure attained during the deposition defines the RRM properties. Now, if the VO₂-substrate interface energy had a role in defining the RRM, we would expect a change in the signal upon thinning, since the ratio between bulk energy and interface energy would change. However, even when thinning to half of the original thickness, the ΔT was not affected. Thus, we conclude that the substrate interaction cannot be a main contributing parameter to the scars' stabilization. However, the growth characteristics of the thin layer, which is controlled also by the substrate, does have an important contribution to the RRM, i.e., the crystal structure, grain size, and amount of strain, which depend also on the substrate, do control the resulting RRM effect.

We found that VO₂ atop SiO₂/Si show upward of 5 times increase in the RRM signal relative to VO₂ grown on C-cut sapphire of similar thicknesses. The grains' size of the VO₂ films on SiO₂/Si are comparable to those grown on sapphire [Fig. 4(e) and Figs. 7(d) and 7(e)] when comparing similar thickness. The main difference of the growth atop SiO₂ is that the VO₂ films do not have any considerable interface strain between the film and the substrate, as there is no lattice matching (only preferred out-of-plane growth direction [40,41], with no in-plane preference), whereas growth atop both R- and C-cut sapphire has lattice matching [32,33,42] and preferred in-plane orientations. We recall that the 120-nm VO₂ film on SiO₂ had additional phases to VO₂ (V₆O₁₃ and V₄O₉). This resulted in a smaller resistance change in the IMT transition (compared to the 60-nm film). Note that the ΔT analysis only measures the changes of the IMT; thus, it is not sensitive (to a first approximation) to the additional phases. However, the observed RRM effect was the largest in this film. The existence of additional phases might influence the RRM in other ways, e.g., scars existing between two VO₂ grains might have a different amount of temperature shift than scars existing between VO₂ and a different phase. In the scope of this study, we cannot assess such contributions.

Taking into consideration all the results discussed above, we understand the situation as follows. Recall that the phase boundaries between phase-separated insulating and metallic domains is where the scars (with increased critical temperature) develop. The underlying mechanism for the scar formation was suggested to be the development of strain at the phase boundaries which are stabilized due to the ramp reversal process [3]. It has been demonstrated that uniaxial strain can significantly shift the transition temperature in VO₂ [20,21,24,25,27,43–45]. We hypothesize that if the interface (and scars) of the phase-separated grains have more possi-

bility to deform, then they can organize in such a way that the stabilizing energy of the scars is greater, which leads to a larger shift of the local critical temperature. Put simply, the more freedom the grains have to reorganize, the more energy will be needed in order to release the scars from the ramp reversal induced stable state. This scenario coincides with the measurement that films grown epitaxially, which are “locked” with the substrate through interface strain, have a much smaller RRM signal than those grown nonepitaxially. In addition, larger grains may have much more strain energy at the interface, which results in a larger energy barrier, relative to smaller grains, where strain can be distributed on many more grain boundaries. This will result in a larger RRM effect for larger grains. The organization of the grains and grain boundaries is defined during the growth of the film. The etch-based thinning process does not change the grain arrangement, and therefore the energy state of the scars will not be affected. Only when the film starts to separate into islands is there more possibility for deformation of the remaining grains, and then an increase in the RRM signal is measured.

Recently, an additional mechanism was suggested for the development of the ramp reversal memory effect [2]. It was proposed that during the phase-separated state there is a diffusion of point defects across the metal insulator boundary, where these defects accumulate in the metal regions and deplete from the insulating ones (defects could include, e.g., oxygen and oxygen vacancies). As defects are transported out of the insulating regions, the T_C of the insulator near the phase boundary increases, while the T_C may also decrease in the metallic regions with higher defect concentration. This model does not directly explain the results we presented herein. However, it is plausible that the strain gradient experienced during the transition contributes to the diffusion of the impurities, introducing a drift term, accelerating the process. Further theoretical analysis is needed to assess if the current study could be understood through the point-defect diffusion model.

We finish the discussion with two final notes. First, the source of the difference between the maximum ΔT and the maximum in the TCR is not clear, especially the larger shift in films deposited on SiO₂ compared to films deposited on sapphire. This could indicate that there is some directionality in the percolation nature of the IMT [31]. We hope that our findings will encourage additional studies to clarify this open question.

Finally, we draw attention to an additional phenomenon that was observed during the etching study of VO₂ on C-cut sapphire. In a previous paper [28], we investigated the effects of the wet-etching process on VO₂ films deposited on R-cut sapphire substrates. The results demonstrated that although the etching process increased the films' roughness somewhat, the thickness remained relatively uniform, i.e., the etching was not directional. In this study, we performed the same etching process on VO₂ films grown on C-cut sapphire substrates, as described in the Results, Sec. II (Fig. 5). Fig. 9 presents a zoom-in of the most etched film (nominally 26 nm). Notably, the etching process exhibits nonuniform behavior in these films, resulting in voids with hexagonal symmetry. This matches with the in-plane symmetry of the C-cut substrates and with the VO₂ grown atop [32], i.e., the VO₂ is preferentially etched to specific planes of the VO₂.

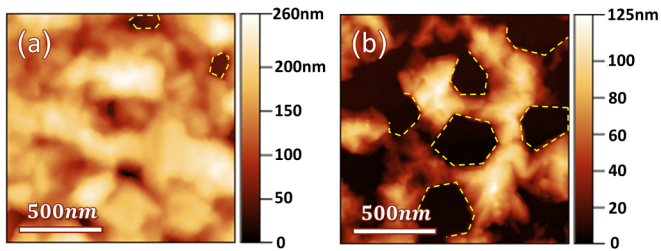


FIG. 9. (a), (b) AFM measurement of the 134-nm (a) and 26-nm (b) postdeposition etched films (from the originally 180-nm film). (a) The 134-nm film is mostly uniform, with small number of voids. The large ones start to show a hexagonal structure. The 26-nm film shows larger voids with a clear distinct hexagonal structure, and a possible order hexagonal structure of the voids.

IV. SUMMARY

To summarize, we have performed an extensive study of the RRM magnitude, and as it is affected by film properties, namely thickness, etching, grain size, and substrate choice. We performed a quantitative measurement of the ΔT magnitude and compare different films, going beyond the qualitative measurements previously reported. The main conclusions are that if the phase-separated grains in the film can relax into a more stable energy state—it will result in a larger RRM

signal, as is exhibited through the amplitude of the measured ΔT . This further corroborates with the fact that the RRM signal grows fivefold when the VO_2 is deposited nonepitaxially atop SiO_2/Si substrates, compared to epitaxial films grown on sapphire substrates. This led to a large ΔT , of nearly 0.6 K change in critical temperature, which can also make the memory effect relevant for applications. We clearly see that more scars do lead to a larger ΔT , as is demonstrated by the magnitude increasing toward the maximum of the TCR, which is close to the percolation threshold of the system, i.e., where there are the most phase boundaries at the reversal temperature. All these data put together do point to strain gradients at the phase boundaries being the leading factor in causing the RRM, but we cannot rule out the recently proposed defect-diffusion model. Any future theoretical descriptions of the effect must be able to reproduce the reported features of the RRM. We hope this and previous papers on RRM will encourage additional experimental and theoretical work to enhance our understanding of this memory effect.

ACKNOWLEDGMENT

This research was supported by The Israel Science Foundation (Grant No. 1499/23).

- [1] N. Vardi, E. Anouchi, T. Yamin, S. Middey, M. Kareev, J. Chakhalian, Y. Dubi, and A. Sharoni, Ramp-reversal memory and phase-boundary scarring in transition metal oxides, *Adv. Mater.* **29**, 1605029 (2017).
- [2] S. Basak, F. Simmons, P. Salev, I. K. Schuller, L. Aigouy, E. W. Carlson, and A. Zimmers, Spatially distributed ramp reversal memory in VO_2 , *Adv. Electron. Mater.* **9**, 2300085 (2023).
- [3] E. Anouchi, N. Vardi, Y. Kalcheim, I. K. Schuller, and A. Sharoni, Universality and microstrain origin of the ramp reversal memory effect, *Phys. Rev. B* **106**, 205145 (2022).
- [4] F. J. Morin, Oxides which show a metal-to-insulator transition at the neel temperature, *Phys. Rev. Lett.* **3**, 34 (1959).
- [5] J. K. Vassiliou, M. Hornbostel, R. Ziebarth, and F. J. DiSalvo, Synthesis and properties of NdNiO_3 prepared by low-temperature methods, *J. Solid State Chem.* **81**, 208 (1989).
- [6] S. Ramanathan, *Thin Film Metal-Oxides: Fundamentals and Applications in Electronics and Energy* (Harvard University: Springer, New York, 2010).
- [7] T. Yao, X. Zhang, Z. Sun, S. Liu, Y. Huang, Y. Xie, C. Wu, X. Yuan, W. Zhang, Z. Wu, G. Pan, F. Hu, L. Wu, Q. Liu, and S. Wei, Understanding the nature of the kinetic process in a VO_2 metal-insulator transition, *Phys. Rev. Lett.* **105**, 226405 (2010).
- [8] P. D. Dernier and M. Marezio, Crystal structure of the low-temperature antiferromagnetic phase of V_2O_3 , *Phys. Rev. B* **2**, 3771 (1970).
- [9] P. H. Xiang, N. Zhong, C. G. Duan, X. D. Tang, Z. G. Hu, P. X. Yang, Z. Q. Zhu, and J. H. Chu, Strain controlled metal-insulator transition in epitaxial NdNiO_3 thin films, *J. Appl. Phys.* **114**, 243713 (2013).
- [10] J. L. García-Muñoz, M. A. G. Aranda, J. A. Alonso, and M. J. Martínez-Lope, Structure and charge order in the antiferromagnetic band-insulating phase of NdNiO_3 , *Phys. Rev. B* **79**, 134432 (2009).
- [11] D. Preziosi, L. Lopez-Mir, X. Li, T. Cornelissen, J. H. Lee, F. Trier, K. Bouzehouane, S. Valencia, A. Gloter, A. Barthélémy, and M. Bibes, Direct mapping of phase separation across the metal-insulator transition of NdNiO_3 , *Nano Lett.* **18**, 2226 (2018).
- [12] A. S. McLeod, E. van Heumen, J. G. Ramirez, S. Wang, T. Saerbeck, S. Guenon, M. Goldfla, L. Andereg, P. Kelly, A. Mueller, M. K. Liu, Ivan K. Schuller, and D. N. Basov, Nanotextured phase coexistence in the correlated insulator V_2O_3 , *Nat. Phys.* **13**, 80 (2017).
- [13] H. T. Stinson, A. Sternbach, O. Najera, R. Jing, A. S. McLeod, T. V. Slusar, A. Mueller, L. Andereg, H. T. Kim, M. Rozenberg, and D. N. Basov, Imaging the nanoscale phase separation in vanadium dioxide thin films at terahertz frequencies, *Nat. Commun.* **9**, 3604 (2018).
- [14] P. Jin and S. Tanemura, Relationship between transition temperature and x in $\text{V}_{1-x}\text{W}_x\text{O}_2$ films deposited by dual-target magnetron sputtering, *Jpn. J. Appl. Phys.* **34**, 2459 (1995).
- [15] M. Jo, H. J. Lee, C. Oh, H. Yoon, J. Y. Jo, and J. Son, Gate-induced massive and reversible phase transition of VO_2 channels using solid-state proton electrolytes, *Adv. Funct. Mater.* **28**, 1802003 (2018).
- [16] J. Jeong, N. Aetukuri, T. Graf, T. D. Schladt, M. G. Samant, and S. S. P. Parkin, Suppression of metal-insulator transition in VO_2 by electric field-induced oxygen vacancy formation, *Science* **339**, 1402 (2013).
- [17] H. Paik, J. A. Moyer, T. Spila, J. W. Tashman, J. A. Mundy, E. Freeman, N. Shukla, J. M. Lapano, R. Engel-Herbert, W. Zander, J. Schubert, D. A. Muller, S. Datta, P. Schiffer, and

- D. G. Schlom, Transport properties of ultra-thin VO₂ films on (001) TiO₂ grown by reactive molecular-beam epitaxy, *Appl. Phys. Lett.* **107**, 163101 (2015).
- [18] K. Han, L. Wu, Y. Cao, H. Wang, C. Ye, K. Huang, M. Motapothula, H. Xing, X. Li, Q. Dong-Chen, X. Li, and X. R. Wang, Enhanced metal-insulator transition in freestanding VO₂ down to 5 nm thickness, *ACS Appl. Mater. Interfaces* **13**, 16688 (2021).
- [19] N. B. Aetukuri, A. X. Gray, M. Drouard, M. Cossale, L. Gao, A. H. Reid, R. Kukreja, H. Ohldag, C. A. Jenkins, E. Arenholz, K. P. Roche, H. A. Dürr, M. G. Samant, and S. S. P. Parkin, Control of the metal-insulator transition in vanadium dioxide by modifying orbital occupancy, *Nat. Phys.* **9**, 661 (2013).
- [20] Y. Muraoka, Y. Ueda, and Z. Hiroi, Large modification of the metal-insulator transition temperature in strained VO₂ films grown on TiO₂ substrates, *J. Phys. Chem. Solids* **63**, 965 (2002).
- [21] S. Yonezawa, Y. Muraoka, Y. Ueda, and Z. Hiroi, Epitaxial strain effects on the metal-insulator transition in V₂O₃ thin films, *Solid State Commun.* **129**, 245 (2004).
- [22] A. J. Sternbach, F. L. Ruta, Y. Shi, T. Slusar, J. Schalch, G. Duan, A. S. McLeod, X. Zhang, M. Liu, A. J. Millis, H. T. Kim, L. Q. Chen, R. D. Averitt, and D. N. Basov, Nanotextured dynamics of a light-induced phase transition in VO₂, *Nano Lett.* **21**, 9052 (2021).
- [23] M. M. Qazilbash, M. Brehm, B. G. Chae, P. C. Ho, G. O. Andreev, B. J. Kim, S. J. Yun, A. V. Balatsky, M. B. Maple, F. Keilmann, H. T. Kim, and D. N. Basov, Mott transition in VO₂ revealed by infrared spectroscopy and nano-imaging, *Science* **318**, 1750 (2007).
- [24] J. Cao, E. Ertekin, V. Srinivasan, W. Fan, S. Huang, H. Zheng, J. W. L. Yim, D. R. Khanal, D. F. Ogletree, J. C. Grossman, and J. Wu, Strain engineering and one-dimensional organization of metal-insulator domains in single-crystal vanadium dioxide beams, *Nat. Nanotechnol.* **4**, 732 (2009).
- [25] T. Kikuzuki and M. Lippmaa, Characterizing a strain-driven phase transition in VO₂, *Appl. Phys. Lett.* **96**, 132107 (2010).
- [26] R. M. Bowman and J. M. Gregg, VO₂ thin films: Growth and the effect of applied strain on their resistance, *J. Mater. Sci. Mater. Electron.* **9**, 187 (1998).
- [27] L. L. Fan, S. Chen, Z. L. Luo, Q. H. Liu, Y. F. Wu, L. Song, D. X. Ji, P. Wang, W. S. Chu, C. Gao, C. W. Zou, and Z. Y. Wu, Strain dynamics of ultrathin VO₂ film grown on TiO₂(001) and the associated phase transition modulation, *Nano Lett.* **14**, 4036 (2014).
- [28] T. Yamin, S. Wissberg, H. Cohen, G. Cohen-Taguri, and A. Sharoni, Ultrathin films of VO₂ on R-cut sapphire achieved by postdeposition etching, *ACS Appl. Mater. Interfaces* **8**, 14863 (2016).
- [29] T. Yamin, T. Havdala, and A. Sharoni, Patterning of epitaxial VO₂ microstructures by a high-temperature lift-off process, *Mater. Res. Express* **1**, 046302 (2015).
- [30] See Supplemental Material at <http://link.aps.org/supplemental/10.1103/PhysRevMaterials.8.015002> including in-depth description of measurement protocol and additional measurements of R-cut sapphire substrates, which includes Refs. [46,47].
- [31] T. Yamin, Y. M. Strelnik, and A. Sharoni, High resolution Hall measurements across the VO₂ metal-insulator transition reveal impact of spatial phase separation, *Sci. Rep.* **6**, 19496 (2016).
- [32] T. H. Yang, C. Jin, R. Aggarwal, R. J. Narayan, and J. Narayan, On growth of epitaxial vanadium oxide thin film on sapphire (0001), *J. Mater. Res.* **25**, 422 (2010).
- [33] T. H. Yang, R. Aggarwal, A. Gupta, H. Zhou, R. J. Narayan, and J. Narayan, Semiconductor-metal transition characteristics of VO₂ thin films grown on c- and r-sapphire substrates, *J. Appl. Phys.* **107**, 053514 (2010).
- [34] K. M. Niang, G. Bai, H. Lu, and J. Robertson, Microstructure scaling of metal-insulator transition properties of VO₂ films, *Appl. Phys. Lett.* **118**, 121901 (2021).
- [35] V. Balakrishnan, C. Ko, and S. Ramanathan, Size effects on stress relaxation across the metal-insulator transition in VO₂ thin films, *J. Mater. Res.* **26**, 1384 (2011).
- [36] B. G. Chae, H. T. Kim, S. J. Yun, B. J. Kim, Y. W. Lee, and K. Y. Kang, Comparative analysis of VO₂ thin films prepared on sapphire and SiO₂/Si substrates by the sol-gel process, *Jpn. J. Appl. Phys.* **46**, 738 (2007).
- [37] M. J. Miller and J. Wang, Influence of grain size on transition temperature of thermochromic VO₂, *J. Appl. Phys.* **117**, 034307 (2015).
- [38] D. Brassard, S. Fourmaux, M. Jean-Jacques, J. C. Kieffer, and M. A. El Khakani, Grain size effect on the semiconductor-metal phase transition characteristics of magnetron-sputtered VO₂ thin films, *Appl. Phys. Lett.* **87**, 051910 (2005).
- [39] A. Kim, S. Y. Lim, J. H. Park, J. S. Chung, H. Cheong, C. Ko, J. G. Yoon, and S. M. Yang, Nanoscale mapping of temperature-dependent conduction in an epitaxial VO₂ film grown on an Al₂O₃ substrate, *RSC Adv.* **12**, 23039 (2022).
- [40] Q. Shi, W. Huang, J. Wu, Y. Zhang, Y. Xu, Y. Zhang, S. Qiao, and J. Yan, Terahertz transmission characteristics across the phase transition in VO₂ films deposited on Si, sapphire, and SiO₂ substrates, *J. Appl. Phys.* **112**, 033523 (2012).
- [41] M. Nagashima and H. Wada, The oxygen deficiency effect of VO₂ thin films prepared by laser ablation, *J. Mater. Res.* **12**, 416 (1997).
- [42] Y. Zhao, J. Hwan Lee, Y. Zhu, M. Nazari, C. Chen, H. Wang, A. Bernussi, M. Holtz, and Z. Fan, Structural, electrical, and terahertz transmission properties of VO₂ thin films grown on c-, r-, and m-plane sapphire substrates, *J. Appl. Phys.* **111**, 053533 (2012).
- [43] Y. Muraoka and Z. Hiroi, Metal-insulator transition of VO₂ thin films grown on TiO₂(001) and (110) substrates, *Appl. Phys. Lett.* **80**, 583 (2002).
- [44] H. Kim, N. A. Charipar, J. Figueroa, N. S. Bingham, and A. Piqué, Control of metal-insulator transition temperature in VO₂ thin films grown on RuO₂/TiO₂ templates by strain modification, *AIP Adv.* **9**, 015302 (2019).
- [45] D. Lee, J. Lee, K. Song, F. Xue, S. Y. Choi, Y. Ma, J. Podkaminer, D. Liu, S. C. Liu, B. Chung, W. Fan, S. J. Cho, W. Zhou, J. Lee, L. Q. Chen, S. H. Oh, Z. Ma, and C. B. Eom, Sharpened VO₂ phase transition via controlled release of epitaxial strain, *Nano Lett.* **17**, 5614 (2017).
- [46] D. Nečas and P. Klapeček, Gwyddion: An open-source software for SPM data analysis, *Cent. Eur. J. Phys.* **10**, 181 (2012).
- [47] G. K. Williamson and W. H. Hall, X-ray broadening from filed aluminium and tungsten, *Acta Metall.* **1**, 22 (1953).